Modeling of an axial injection torch

L.L. Alves[1], R. Álvarez[1], L. Marques[1,2], S.J. Rubio[3], A. Rodero[3], and M.C. Quintero[3]

[1] Instituto de Plasmas e Fusão Nuclear, Instituto Superior Técnico, Av. Rovisco Pais, 1049-001 Lisboa, Portugal

[2] Centro de Física da Universidade do Minho, Universidade do Minho, 4710-057 Braga, Portugal

[3] Departamento de Física, Universidad de Córdoba, Campus Universitario de Rabanales, Spain

Abstract. This paper presents simulation results for a microwave (2.45 GHz) plasma reactor, operated by an axial injection torch (AIT). The study gives a two-dimensional description of the AIT-reactor system, based on an electromagnetic model (that solves Maxwell's equations adopting a harmonic time description, yielding the distribution of the electromagnetic fields and the average power absorbed by the plasma), and a hydrodynamic model (that solves the Navier-Stokes equations for the flowing neutral gas, yielding the distribution of mass density, pressure, temperature, and velocities). Comparison between model results and experimental measurements reveal common variation trends, with changes in the reactor height, for the power reflected by the system, and yield a qualitative agreement for the axial profile of the gas rotational temperature. Model results, such as the power transmission coefficient and the gas temperature, are particularly dependent on the reactor dimensions, the electron density and temperature, and the gas input flow, which indicates that simulations can be used to provide general guidelines for device optimization.

PACS. 52.75.Hn Plasma torches – 52.50.Sw Plasma heating by microwaves; ECR, LH, collisional heating – 52.30.-q Plasma dynamics and flow

1 Introduction

An Axial Injection Torch (AIT) [1–9] is a microwave-driven atmospheric plasma source that operates in different pure gases (helium, argon, nitrogen) or gas mixtures (e.g. air), over a wide range of powers ($300 - 3000$ W) and flow-rates ($0.5 - 13$ L min^{-1}). The AIT can produce very hot flows of plasma species, hence being used in gas heat-

---

ing applications, industrial material processing, chemical processing, and environmental control.

This paper presents simulation results for a microwave-driven ($\omega/2\pi = 2.45$ GHz) plasma reactor, operated by an AIT. The particular device under study couples the AIT (connected to a coaxial waveguide with inner and outer radial dimensions $R_i = 5.3$ mm and $R_o = 14.5$ mm, respectively) to a cylindrical reactor chamber (with $R = 55$ mm radius and $L = 150$ mm height), where it produces a helium plasma at atmospheric pressure (Spanish patents P200201328 and P200302980). Figure 1 represents a scale diagram of this device, where the portion of the nozzle inside the reactor measures $l_n = 15$ mm and the length of the nozzle's tip is $l_t = 10$ mm. The work is part of a modeling strategy, aiming the development of a modular simulation tool for the integrated description of an AIT-reactor system, from the power injection and coupling to the plasma production and transport, under a gas flow regime. Our interest goes from the mere prediction of working characteristics to device optimization (based on a deep knowledge of the processes within the plasma), for example in view of a high-performance heat transfer and/or an enhanced chemical reactivity.

Here, we focus on the following two-dimensional (2D) simulation modules: (i) electromagnetic (EM) module [10–12], yielding the distribution of the EM fields and the average power absorbed by the plasma; (ii) hydrodynamic (HD) module [13] for the neutral gas (accounting for the collisional heat transfer in the presence of plasma), yielding the distribution of its mass density, pressure, temper-

ature, and (axial and radial) velocities. Both EM and HD models are solved given the 2D profiles of the electron density n_e (with maximum values $n_{e,\max} = 10^{14} - 2 \times 10^{15}$ cm^{-3}) and temperature T_e (with a maximum value $T_{e,\max} = 2 \times 10^4$ K), which are defined according to optical emission spectroscopy measurements [2,5,7,8]. We have assumed a plasma with 0.5 mm radius and 20 mm height, imposing an axial linear decrease for both n_e and T_e, from their maximum values. Figures 2(a)-(b) plot the radial profiles of the electron density and temperature, respectively. As shown, we have considered several types of radial variations for n_e (termed hollow, displaced hollow, flat, linear), to study their influence on results. These empirical profiles are used to tailor both the plasma conductivity (within the EM model, via the electron density) and the gas heating term (within the HD model, via the electron density and temperature).

2 Electromagnetic module

2.1 Maxwell's equations

The EM module [10–12] solves Maxwell's equations to calculate the 2D distribution of the EM fields inside the AIT-reactor system, and the average power absorbed by the plasma. The coaxial (TEM) excitation pattern, combined with the axis-symmetric geometry of the device, supports the assumption that the EM field distribution inside the reactor is a linear combination of TM$_{0m}$ modes, with no dependence on the azimuthal angle. With these suppositions, and by further adopting a harmonic time descrip-

tion [14], Maxwell's equations are written in cylindrical coordinates as

$$\frac{\partial E_z}{\partial r} - \frac{\partial E_r}{\partial z} = \frac{ik_0}{\sqrt{\varepsilon_0/\mu_0}} \frac{rH_\varphi}{r} \qquad (1)$$

$$\frac{1}{r}\frac{\partial(rH_\varphi)}{\partial r} = ik_0\varepsilon\sqrt{\frac{\varepsilon_0}{\mu_0}}E_z \qquad (2)$$

$$\frac{1}{r}\frac{\partial(rH_\varphi)}{\partial z} = -ik_0\varepsilon\sqrt{\frac{\varepsilon_0}{\mu_0}}E_r \quad . \qquad (3)$$

Here, $E_r(r,z)$ and $E_z(r,z)$ are the complex radial and axial electric field components, respectively; $H_\varphi(r,z)$ is the complex azimuthal magnetic field; ε_0 and μ_0 are the vacuum electric permittivity and magnetic permeability, respectively; $k_0 \equiv \omega/c$ (c is the vacuum speed of light); $\varepsilon(r,z)$ is the relative permittivity of the background medium [for the neutral gas $\varepsilon = 1$; for the plasma $\varepsilon = 1 - i\sigma/(\omega\varepsilon_0) \simeq 1 - \omega_p^2/[\omega(\omega - i\nu)]$ [15], with σ the electron plasma conductivity, $\omega_p \equiv (n_e e^2/\varepsilon_0 m_e)^{1/2}$ the electron plasma frequency (e and m_e are the electron charge and mass, respectively), and $\nu = 6.8 \times 10^{-8} n_g$ s^{-1} the electron-neutral collision frequency [16] (n_g is the gas density in cm^{-3})].

2.2 Boundary conditions

Equations (1)-(3) are solved subject to the following boundary conditions. At the reactor axis ($r = 0$), the symmetry condition $H_\varphi = 0$ is applied. Perfect-conductor conditions are imposed at the reactor metal boundaries, by setting $E_r = 0$ at horizontal walls and $E_z = 0$ at vertical walls. In practice, because we are solving a discrete equation system for the magnetic field (see Sect. 2.4), these Dirichlet conditions on E_r and E_z are better rewritten as Neumann

conditions on rH_φ [see Eqns. (1)-(3)]:

$$E_{r_{\text{horiz walls}}} = 0 \rightarrow \frac{\partial(rH_\varphi)}{\partial z}\bigg|_{\text{horiz walls}} = 0 \qquad (4)$$

$$E_{z_{\text{vert walls}}} = 0 \rightarrow \frac{\partial(rH_\varphi)}{\partial r}\bigg|_{\text{vert walls}} = 0 \quad . \qquad (5)$$

However, numerical tests show that the direct imposition of boundary conditions (4)-(5) doesn't restrict the solution, thus leading to a numerical divergence. This problem occurs for reactor radii above the critical value $R_c \simeq 47$ mm (at 2.45 GHz frequency), when a wave-mode solution develops, similarly to what is observed in air-filled, one-end-shorted circular waveguides [10–12,17,18]. To circumvent this difficulty, we have replaced the Neumann condition (5), at $r = R$, with an equivalent Dirichlet-type boundary condition on rH_φ. The latter is tailored using a Newton-Raphson iterative algorithm, according to which the values of $RH_\varphi(R,z)$ follow a convergence path towards the physical solution $E_z(R,z) = 0$. Details on the numerical algorithm adopted can be found in [12].

At the excitation plane (located at the lower open-end of the coaxial waveguide, see Fig. 1), an absorbing boundary condition (ABC) is considered in order to eliminate non-physical reflections, coming from the modeling of the waveguide as a finite system [14,19–24]. For a H_φ^- component, associated with a reflected plane-wave propagating towards the excitation plane (i.e. along direction $-\mathbf{e}_z$), the first-order ABC writes (for a harmonic time description) [20]

$$\frac{\partial H_\varphi^-}{\partial z}\bigg|_{\text{exc plane}} - ik_0 H_\varphi^-{}_{\text{exc plane}} = 0 \quad . \qquad (6)$$

This boundary condition yields perfect absorption for a normal incidence of the reflected wave [i.e. for a H_φ^- com-

ponent as similar as possible to a (reflected) TEM plane-wave], which is ensured by moving the excitation plane away from the cylindrical reactor. In practice, $H^-_{\varphi\,\mathrm{exc\,plane}}$ is generally defined as

$$H^-_{\varphi\,\mathrm{exc\,plane}} \equiv H_{\varphi\,\mathrm{exc\,plane}} - H^+_{\varphi\,\mathrm{exc\,plane}}, \qquad (7)$$

where $H_{\varphi\,\mathrm{exc\,plane}}$ is the calculated magnetic field at the excitation plane and $H^+_{\varphi\,\mathrm{exc\,plane}}$ relates to the magnetic field with the coaxial waveguide, associated to a TEM wave propagating towards the reactor (i.e. along direction $\mathbf{e}_z$) [17,18]

$$H^+_{\varphi\,\mathrm{exc\,plane}} \equiv H^{\mathrm{TEM}}_{\varphi} \propto \frac{\exp\left[-ik_0 z_{\mathrm{exc\,plane}}\right]}{r} \quad . \qquad (8)$$

2.3 Power balance

The quality of power coupling for the AIT-reactor system is measured by its power transmission coefficient [17]

$$\frac{P_{\mathrm{abs}}}{P_0} \equiv \frac{\frac{1}{2}\int_V \Re[\sigma]\,|E|^2\,dV}{\frac{1}{2}\Re\int_{\mathrm{exc.\,plane}} E^{\mathrm{TEM}}_r (H^{\mathrm{TEM}}_{\varphi})^\star\,dS} \quad , \qquad (9)$$

where $|E|^2 \equiv |E_r|^2 + |E_z|^2$ is the total electric field, P_{abs} is the time-average power absorbed by the plasma, and P_0 is the time-average incident power on the excitation plane, which is an input parameter to the model ($\Re$ represents *the real part of* and $\star$ refers to the complex conjugate).

2.4 Numerics

Maxwell's equations are discretized onto a 2D, non-uniform grid, using a technique based on Yee's method [25]. Grid design follows the reactor geometry, with a point-density that increases near regions where either the plasma parameters or the field components are expected to present steep variations (e.g. at the nozzle's tip, in the plasma region, and near the reactor walls). The number of grid points (typically 10^4) is set as to provide both numerical accuracy and a proper description of the plasma region, while ensuring acceptable run times ($\sim$ 10 min-3 hrs on a 2.5 GHz CPU, depending on the number of grid points). After discretization, Maxwell's equations are merged into a Helmholtz-type equation in the single quantity rH_{φ}. The discretized equation is solved using a Gauss-Seidel iterative algorithm, with a stabilization improvement that uses direct column- and row-wise solutions, and a convergence acceleration that adopts the successive over-relaxation technique [26]. The convergence test checks for a maximum relative error of H_{φ} smaller than 10^{-7}.

2.5 Results and discussion

The EM model is applied to the AIT-reactor system, for various R and L dimensions, at $P_0 = 1$ W and $n_{e,\mathrm{max}} = 10^{15}$ cm^{-3}. Figure 3 presents contour-plots of the modulus of the EM field components (normalized to their maximum values), obtained adopting the hollow radial profile of n_e [see Fig. 2(a)], for $L = 150$ mm and $R = 35$ mm [Figs. 3(a)-(c)] or $R = 55$ mm [Figs. 3(d)-(f)]. The results in these figures show that the AIT-reactor system exhibits features similar to those of an air-filled circular waveguide, shorted by a top metal plate, due to the size of the cylindrical reactor when compared to either the AIT or the plasma small dimensions. Hence, for $R < R_c$ the (evanescent) fields decrease exponentially along the axis,

whereas for $R > R_c$ the fields have an oscillating behavior in axial direction.

Figures 4(a)-(b) plot the axial and radial profiles of the EM field components near the plasma region. Results show that, as expected, E_z is the on-axis dominant EM component [see Fig. 4(a)], exhibiting an axial profile that increases inside the plasma up to its boundary, due to the development of an electron-plasma resonance. This phenomenon is associated with the axial decrease in the electron density, which causes a decrease in ω_p leading to $\Re[\varepsilon_p] \simeq 0$ at resonance position [see Eqns. (1)-(3)]. Notice that, outside the plasma region, E_z exhibits an evanescent behavior up to ~ 61 mm, corresponding approximately to half-wavelength $\pi c/\omega$. At the plasma radial boundary $E_z/E_r \simeq 9$ [see Fig. 4(b)], which is compatible with a skin depth of about $\delta \simeq 9/k_0 \simeq 18$ cm. Thus, for the n_e profile adopted here, the E_z component is able to penetrate the plasma region (exhibiting a quasi-constant value down to the reactor axis), even for a high electron density (hence conductivity) responsible for a vacuum-to-plasma drop in the E_r component.

The previous results give a strong indication that the system dimensions might also influence the fractional average power absorbed by the plasma. Figures 5(a)-(b) plot the calculated power transmission coefficient P_{abs}/P_0 [see Eqn. (9)], as a function of R (at fixed $L = 150$ mm) and L (at fixed $R = 50, 55, 60$ mm), respectively, for different n_e radial profiles at $n_{e,\mathrm{max}} = 10^{15}$ cm^{-3}. Figure 5(b) plots also measured values of $1 - P_{\mathrm{ref}}/P_0$ (where P_{ref} is the reflected power), as a function of L, obtained at $P_0 = 600$ W

and $R = 50$ mm. The results in these figures show that power coupling is strongly affected by variations in both R and L, due to the development of resonant wave-cavity modes. Notice that the radial profile of n_e is not without influence upon power coupling, particularly at small R's and L's for which the plasma starts to modify the overall EM field distribution. With this respect, the non-physical linear profile of n_e limits considerably the absorption of power by the plasma. Moreover, numerical tests reveal that increasing $n_{e,\mathrm{max}}$ leads to more intense maxima, for smaller R and L values. The measured transmission coefficient exhibits the same variation trend with L as the calculated ones, although with less pronounced peaks, in part due to the absorption of energy by the metal waveguides. Notice that P_{ref} was measured at the input of the (finite) coaxial waveguide (not at the reactor entrance), where the sole stubb of the transmission line was tuned as to ensure a maximum coupled power for a reactor with 50 mm radius and 70 mm height. These facts can explain the poor agreement between simulations and experiment. Firstly, $1 - P_{\mathrm{ref}}$ is only a representation of the absorbed power, as the impedance of the coaxial waveguide might have also be affected by changes in L and R. Secondly, the system was tuned to yield a maximum power coupled under different conditions than those predicted by the model. With this respect, the calculated curve of P_{abs}/P_0 vs L can be altered by modifying the *tuning parameter* R within the model. Simulations obtained for $R = 50, 60$ mm [see 5(b)] show a strong modification (both in position and width) of the resonant absorption peaks, leading to predictions

that are closer to measurements when $R = 60$ mm. In any case, measurements confirm that device optimization can be achieved by adjusting its dimensions, as suggested by simulations.

3 Hydrodynamic module

3.1 Navier-Stokes' equations

The HD module [13] solves the Navier-Stokes equations [27, 28] for the flowing neutral gas (including its thermal balance equation), to calculate the 2D distribution of the (axial and radial) velocities $\mathbf{v} \equiv \mathbf{v}_r + \mathbf{v}_z$, mass density $\rho \equiv n_g M_g$ (with M_g the gas molecular mass), pressure $p = n_g k_B T_g$ (with k_B the Boltzmann's constant), and temperature T_g within the reactor. The Navier-Stokes equations write

$$\nabla \cdot (\rho \mathbf{v}) = 0 \tag{10}$$

$$\nabla \cdot (\rho \mathbf{v}\mathbf{v}) = -\nabla p - \nabla \cdot \pi + n_g \mathbf{F} \tag{11}$$

$$\rho C_p (\mathbf{v} \cdot \nabla) T_g = \nabla \cdot (\lambda_g \nabla T_g) - p\nabla \cdot \mathbf{v}$$
$$+ \frac{3}{2}\frac{m_e}{M_g}n_e \nu k_B (T_e - T_g) \quad , \tag{12}$$

where

$$\pi \equiv -\eta \left[\nabla \mathbf{v} + (\nabla \mathbf{v})^T - \frac{2}{3}\nabla \cdot \mathbf{v}\mathbf{I}\right] \tag{13}$$

is the viscosity tensor (with $\eta \simeq C T_g^{1/2} \simeq 4.5 \times 10^{-5}$ Pa s the viscosity coefficient for helium at $T_g \simeq 10^3$ K [29], C a constant, and $\mathbf{I}$ the identity tensor); $\mathbf{F} \equiv M_g\mathbf{g}$ is the gravity force (with $\mathbf{g}$ the corresponding acceleration); $C_p = (5/2)(k_B/M_g)$ is the gas heat capacity and $\lambda_g = (15/4)\eta(k_B/M_g)$ is the gas thermal conductivity [29].

Equations (10)-(12) are solved for input gas flows $Q = 10^2 - 10^4$ sccm, considering that the ratio of the gas input to the gas output surfaces is about 1% (for a nozzle radius $R_{\text{nozz}} = 0.5$ mm). Under these work conditions, the maximum input gas velocity is $v_0 = (0.1/273)(M_g/k_B)$ $(Q/\rho_0)/(60\pi R_{\text{nozz}}^2) \simeq 8 \times 10^4$ cm s^{-1} (for a mass density $\rho_0 = 4.87 \times 10^{-5}$ g cm^{-3} at $T_g \simeq 10^3$ K), which yields a Mach number ($c_s = 1.9 \times 10^5$ cm s^{-1} is the speed of sound in helium at $T_g \simeq 10^3$ K) M $\equiv v_0/c_s \stackrel{<}{\sim} 0.4$ (hence a subsonic flow regime), and a Reynold number Re $\equiv \rho_0 v_0 2R_{\text{nozz}}/\eta \stackrel{<}{\sim} 840$ (hence a non-turbulent flow regime).

3.2 Boundary conditions

Equations (10)-(12) are solved subject to the following boundary conditions. At the reactor axis ($r = 0$) we impose the symmetry conditions $v_r = 0$, $\partial v_z/\partial r = 0$, and $\partial T_g/\partial r = 0$. At reactor walls $\mathbf{v} = 0$ is applied, corresponding to a combination of no-slip conditions (setting to zero all velocity components parallel to walls) with flux conservation conditions (setting to zero all velocity components perpendicular to walls); we also impose the gas temperature at the reactor walls, by setting $T_g = T_{g_w}$. At the input opening (located at $z = l_n$) we give the gas flow $\rho v_z = \rho_0 v_0$; at the output opening (located at $z = L$) we impose the pressure closure condition $p = p_{\text{atm}}$, along with the continuity conditions $\partial v_z/\partial z = 0$ and $\partial T_g/\partial z = 0$. At the nozzle's surface and at the upper wall, additional continuity conditions for the gas temperature are also set, by

imposing $\partial T_g / \partial x_\perp = 0$, where $x_\perp$ is any r, z direction perpendicular to these boundaries.

3.3 Numerics

The Navier-Stokes' equations are discretized onto 2D staggered, cell-centered grids (similar to those adopted in the EM module), using a finite volume method based on surface integrals. Because we are in a subsonic, non-turbulent flow regime, the equations are solved by using the standard SIMPLE algorithm [27], checking for pressure corrections, mass density conservation errors, and T_g relative errors smaller than 10^{-7}. For a 10^4 point grid, the run times are about 5 hrs on a 2.5 GHz CPU.

3.4 Results and discussion

The HD model is applied to the AIT-reactor system, for the radial profiles of n_e and T_e depicted in Fig. 2, at various Q, T_{g_w} and $n_{e,\mathrm{max}}$. Figure 6 presents a contour-plot of the modulus of the total velocity with the flowing gas (normalized to its maximum value), calculated for $Q = 10^3$ sccm and $T_{g_w} = 300$ K, adopting the hollow radial profile of the electron density at $n_{e,\mathrm{max}} = 10^{15}$ cm^{-3}. Results reveal that the gas flow exhibits a vortex, caused by its interaction with the reactor's upper wall. Numerical tests show that this effect spreads over the entire reactor at lower input flows, for which the radial velocity component increases (yielding a gas flow less-oriented towards the output opening) and the vortex moves away from the upper wall.

Figures 7(a)-(b) present a contour-plot of the gas temperature, calculated adopting the hollow radial profile of the electron density at $n_{e,\mathrm{max}} = 10^{15}$ cm^{-3}, $Q = 10^3$ sccm, and $T_{g_w} = 300, 600$ K, respectively. In these figures, the T_g distribution near the nozzle constitutes an indirect image of the plasma, given by the electron energy collisional transfer, as described by the source term $(3/2)(m_e/M_g)$ $n_e \nu k_B (T_e - T_g)$ in Eqn. (12). As expected, results show that the gradients of T_g are strongly attenuated by increasing the gas temperature at the reactor walls.

Figures 8(a)-(b) plot axial and radial T_g profiles, respectively, calculated for $Q = 10^3$ sccm and $T_{g_w} = 300$ K, adopting different n_e radial profiles at $n_{e,\mathrm{max}} = 10^{15}$ cm^{-3}. Figure 8(a) plots also measured values of the gas rotational temperature, obtained at $P_0 = 600$ W from (radially averaged) optical emission spectroscopy diagnostics of the N$_2$ first negative system. Good qualitative agreement is found between simulations and experiment, but the measured T_g is a factor of 1.3 above the calculated one. This difference is probably related to the maximum electron temperature adopted in calculations ($T_{e,\mathrm{max}} = 2 \times 10^4$ K), which seems underestimated with respect to recent Thomson Scattering measurements [30]. Numerical tests do show that the peak of T_g increases by a factor of 1.2 when considering $T_{e,\mathrm{max}} = 3 \times 10^4$ K instead. Figures 8(a)-(b) reveal that the gas temperature features a hollow spatial distribution (in both axial and radial directions) near the nozzle's tip, whose depth relates to the energy relaxation length with the plasma-gas heat transfer. Therefore, the profile of T_g is highly affected by changes in the distribution of the elec-

tron energy density $n_e T_e$ [which accounts for smaller T_g's when adopting a (non-physical) linear decrease for the radial profile of n_e], or in the gas input flow (whose increase leads to longer energy relaxation lengths in axial direction, causing a drop in the peak of T_g, within plasma region, followed by an increase in its tail). These observations reveal that the gas temperature profile can be tailored by modifying the nozzle's design, via changes in either the plasma features or the flow conditions.

4 Final remarks

We have developed two simulation modules, for the two-dimensional description of a microwave plasma reactor, operated by an axial injection torch (AIT). An electromagnetic (EM) module, which solves Maxwell's equations adopting a harmonic time description, yielding the distribution of the electromagnetic fields and the average power absorbed by the plasma; a hydrodynamic (HD) module, which solves the Navier-Stokes equations for the flowing neutral gas, yielding the distribution of mass density, pressure, temperature, and velocities.

The EM results showed that the AIT-reactor system exhibits features similar to those of an air-filled circular waveguide with a shortening metal plate at the top, supporting evanescent or oscillatory solutions for radial dimensions below or above a critical ~ 47 mm radius (at 2.45 GHz), respectively. For the work conditions considered here, the EM fields were found maximum in the plasma region near the nozzle's tip (due to the development of an electron-plasma resonance phenomenon), fea-

turing an axial electric field component that was able to penetrate the plasma region (regardless of the high electron density, hence conductivity). Results have also shown that the fractional average power absorbed by the plasma is strongly influenced by the electron density profile and the system dimensions (the reactor's radius R and height L), thus confirming the role of the latter in defining the EM field distribution pattern. The experimental power transmission coefficient (obtained from measurements of the power reflected by the system) exhibits the same variation trend with L as the calculated one, indicating the development of resonant wave-cavity modes.

The HD results revealed that the gas flow exhibits a vortex, caused by its interaction with the reactor's upper wall, whose position depends strongly on the gas input velocity. Moreover, the calculated gas temperature presented hollow profiles (in both axial and radial directions) near the nozzle's tip, related to the gas input flow and to the spatial distribution of the electron density and temperature. A qualitative agreement is found, along the reactor axis, between model predictions for the gas temperature and measured values of the gas rotational temperature (obtained by radially averaged optical emission spectroscopy diagnostics of the N_2 first negative system), with experiment overestimating simulations by a factor of only 1.3.

In general, model results are particularly dependent on the reactor dimensions, the electron density and temperature, and the gas input flow. This indicates that simulations can assist the optimization of the AIT-reactor

design, in terms of both reactor dimensions, as to ensure a maximum power coupling, and nozzle characteristics, as to control the flow features and provide an adequate gas temperature distribution. However, the full analysis of this problem requires a self-consistent description of the AIT-reactor system, including its electromagnetic excitation, the production of plasma, and the hydrodynamic transport of charged and neutral species. Work is in progress to upgrade the present model version, by coupling the EM and HD modules to a discharge plasma module, in view of constructing an integrated simulation tool.

References

1. M. Moisan, G. Sauvé, Z. Zakrzewski, J. Hubert, Plasma Sources Sci. Technol. **3**, 584 (1994)

2. A. Rodero, M.C. Quintero, A. Sola, A. Gamero, Spectrochim. Acta Part B **51**, 467 (1996)

3. A. Rodero, M.C. García, M.C. Quintero, A. Sola, A. Gamero, J. Phys. D: Appl. Phys. **29**, 681 (1996)

4. J. Jonkers, J.M. de Regt, J.A.M. van der Mullen, H.P.C. Vos, F.P.J. de Groote, E.A.H. Timmermans, Spectrochim. Acta Part B **51**, 1385 (1996)

5. J. Jonkers, L.J.M. Selen, J.A.M. van der Mullen, E.A.H. Timmermans, D.C. Schram, Plasma Sources Sci. Technol. **6**, 533 (1997)

6. M.C. Quintero, A. Rodero, M.C. García, A. Sola, Appl. Spectrosc. **51**, 778 (1997)

7. E.A.H. Timmermans, I.A.J. Thomas, J. Jonkers, J.A.M. van der Mullen, D.C. Schram, Fresenius J. Anal. Chem. **362**, 440 (1998)

8. R. Álvarez, M.C. Quintero, A. Rodero, Spectrochim. Acta Part B **59**, 709 (2004)

9. S. Rubio, A. Rodero, M.C. Quintero, R. Álvarez, C. Lao, A. Gamero, Acta Phys. Slov. **54**, 125 (2004)

10. R. Álvarez, L.L. Alves, J. Appl. Phys. **101**, 103303 (2007)

11. R. Álvarez, L.L. Alves, IEEE Trans. Plasma Science, special issue Images in Plasma Science (in press, September 2008)

12. R. Álvarez, L.L. Alves, J. Phys. D: Appl. Phys. (accepted for publication, 2008)

13. R. Álvarez, L.L. Alves, in *Proceedings of the XIX Europhysics Conference on Atomic and Molecular Physics of Ionised Gases* (Granada, Spain, 2008).

14. A.M. Bilgic, K. Garloff, E. Voges, Plasma Sources Sci. Technol. **8**, 325 (1999)

15. M.A. Lieberman, A.J. Lichtenberg, *Principles of Plasma Discharges and Materials Processing* (John Wiley, New York, 1994)

16. L.L. Alves, C.M. Ferreira, J. Phys. D: Appl. Phys. **24**, 581 (1991)

17. C.C. Johnson, *Field and Wave Electrodynamics* (McGraw-Hill, New York, 1965)

18. R.E. Collin, *Foundations for Microwave Engineering* (McGraw-Hill, New York, 1966)

19. E.L. Lindman, J. Comput. Phys. **18**, 66 (1975)

20. B. Engquist, A. Majda, Math. Comp. **31**, 629 (1977)

21. G. Mur, IEEE Trans. Electromagn. Compat. **23**, 377 (1981)

22. R.L. Higdon, Math. Comp. **47**, 437 (1986)

23. R.L. Higdon, Math. Comp. **49**, 65 (1987)

24. G. Mur, IEEE Trans. Electromagn. Compat. **40**, 100 (1998)

25. K.S. Yee, IEEE Trans. Antennas Propag. **14**, 302 (1966)

26. *Numerical Recipes in C*, edited by W.H. Press et al (Cambridge University Press, Cambridge, 1988)

27. J.H. Ferziger, M. Peric, *Comput. Methods for Fluid Dynamics*, (Springer-Verlag, 1999)

28. Y. Kabouzi, D.B. Graves, E. Castaños-Martínez, M. Moisan, Phys. Rev. E **75**, 016402 (2007)

29. J.O. Hirschfelder, C.F. Curtiss, R.B. Bird, *Molecular Theory of Gases and Liquids* (John Wiley, 1964)

30. S.J. Rubio, A. Rodero, M.C. Quintero, in *Proceedings of the XIX Europhysics Conference on Atomic and Molecular Physics of Ionised Gases* (Granada, Spain, 2008).

Acknowledgments
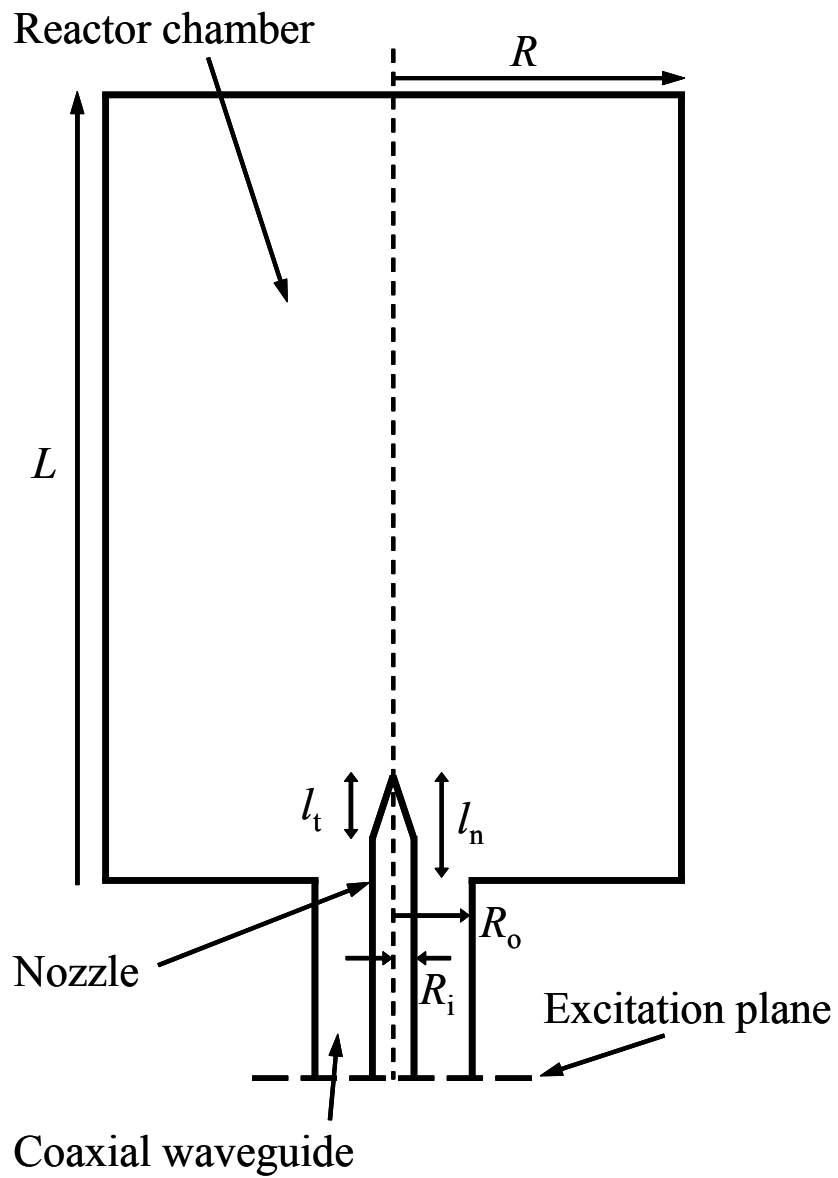
Fig. 1. Schematic scale diagram of the AIT-reactor device. Dimensions are $R_i = 5.3$ mm, $R_o = 14.5$ mm, $l_n = 15$ mm, $l_t = 10$ mm, $R = 55$ mm, and $L = 150$ mm.
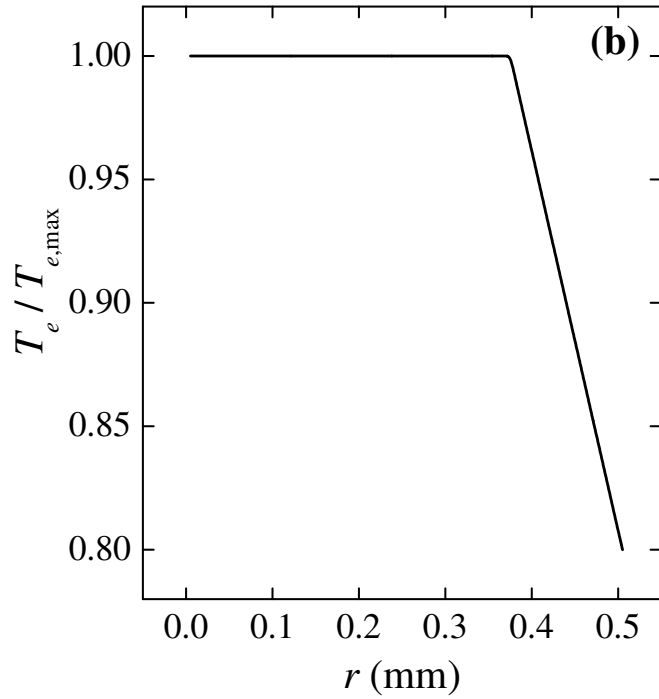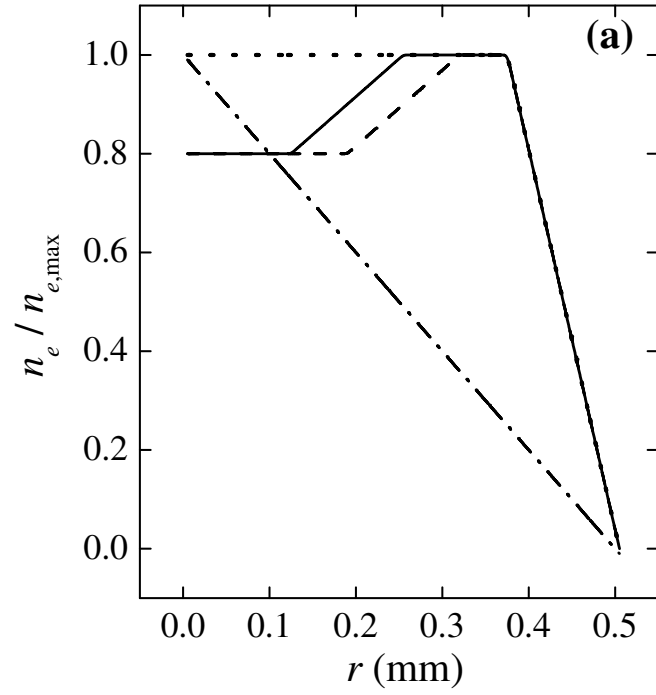
Fig. 2. Radial profiles of the plasma electron density (a) and temperature (b) adopted in simulations. For n_e, the following profiles are considered: hollow (solid curve), displaced hollow (dashed), flat (dotted), and linear (dashed-dotted).
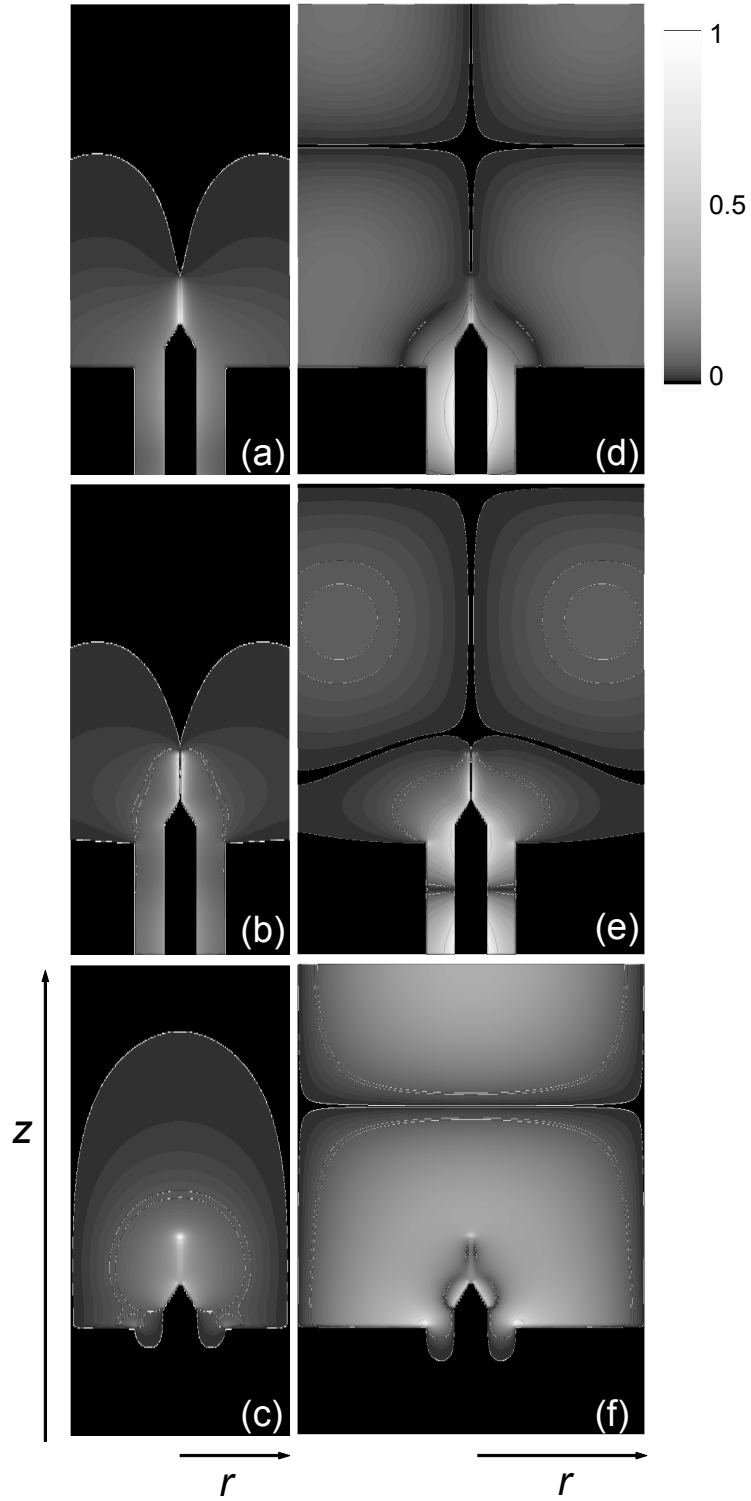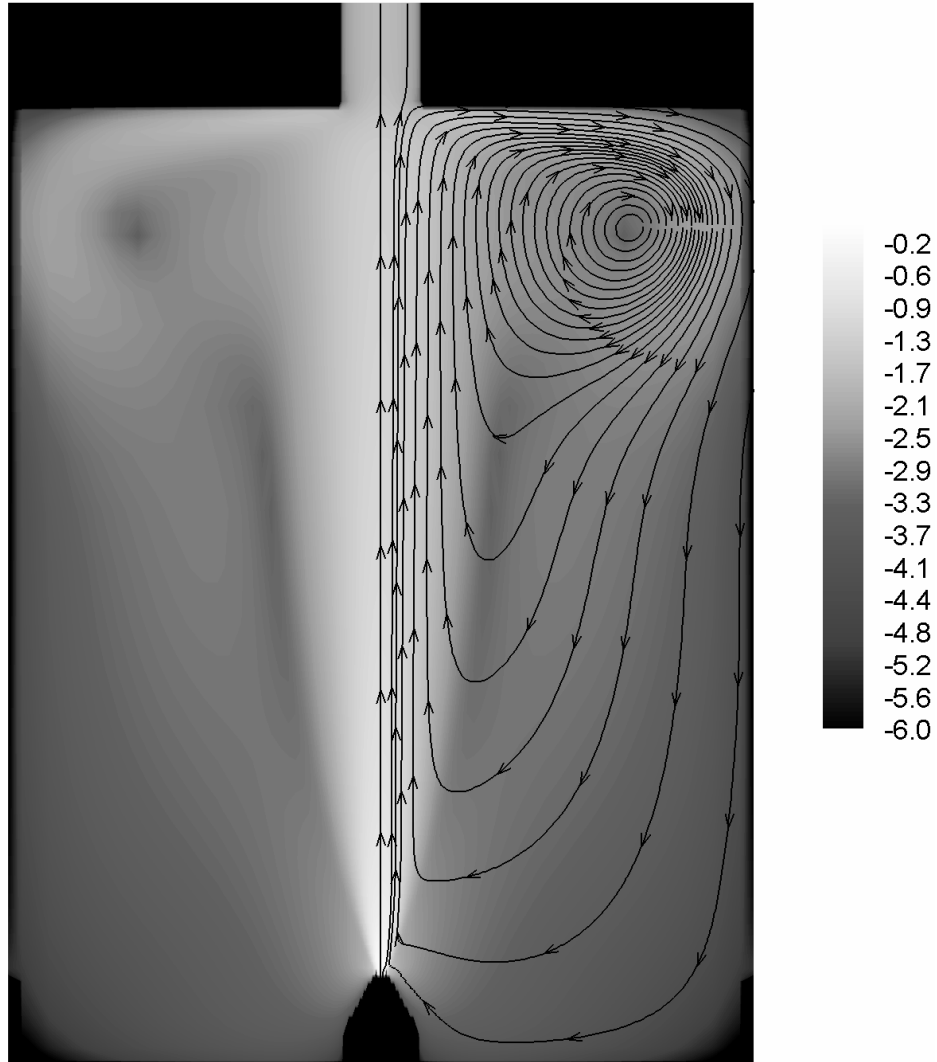
Fig. 3. Contour-plot of the modulus of the EM field components (normalized to their maximum values), numerically calculated for the AIT-reactor represented in Fig. 1, adopting the hollow radial profile of the electron density [see Fig. 2(a)] at $n_{\mathrm{e,max}} = 10^{15}$ cm^{-3}. Results are for the following radius and field components: $R = 35$ mm and H_φ (a), E_r (b), E_z (c); $R = 55$ mm and H_φ (d), E_r (e), E_z (f).
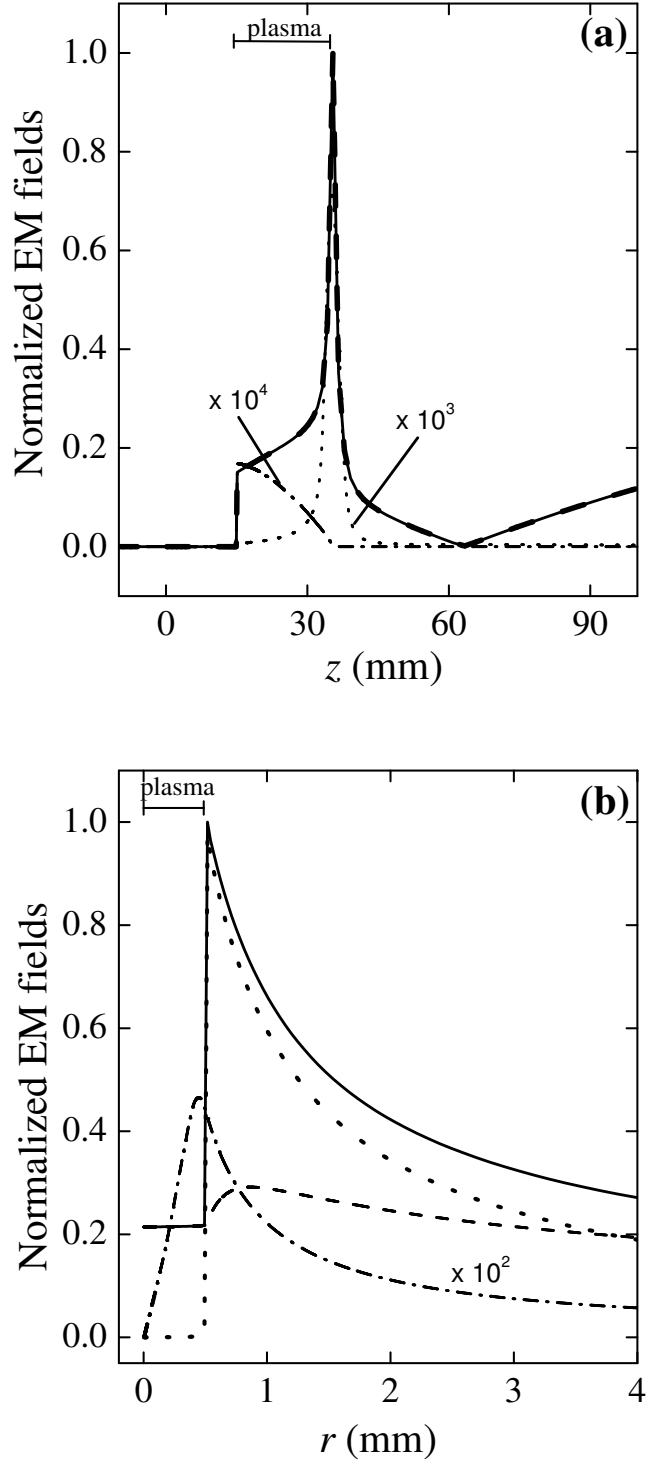
Fig. 4. Calculated axial (at $r = 0^+$) (a) and radial (at $z = l_n^+$) (b) profiles of the modulus of the EM field components (normalized to the maximum of the total electric field E) near the plasma region, obtained adopting the hollow radial profile of the electron density [see Fig. 2(a)] at $n_{\mathrm{e,max}} = 10^{15}$ cm^{-3}. Results are for the following field components: E (solid curves), E_z (dashed), E_r (dotted), H_φ (dashed-dotted).
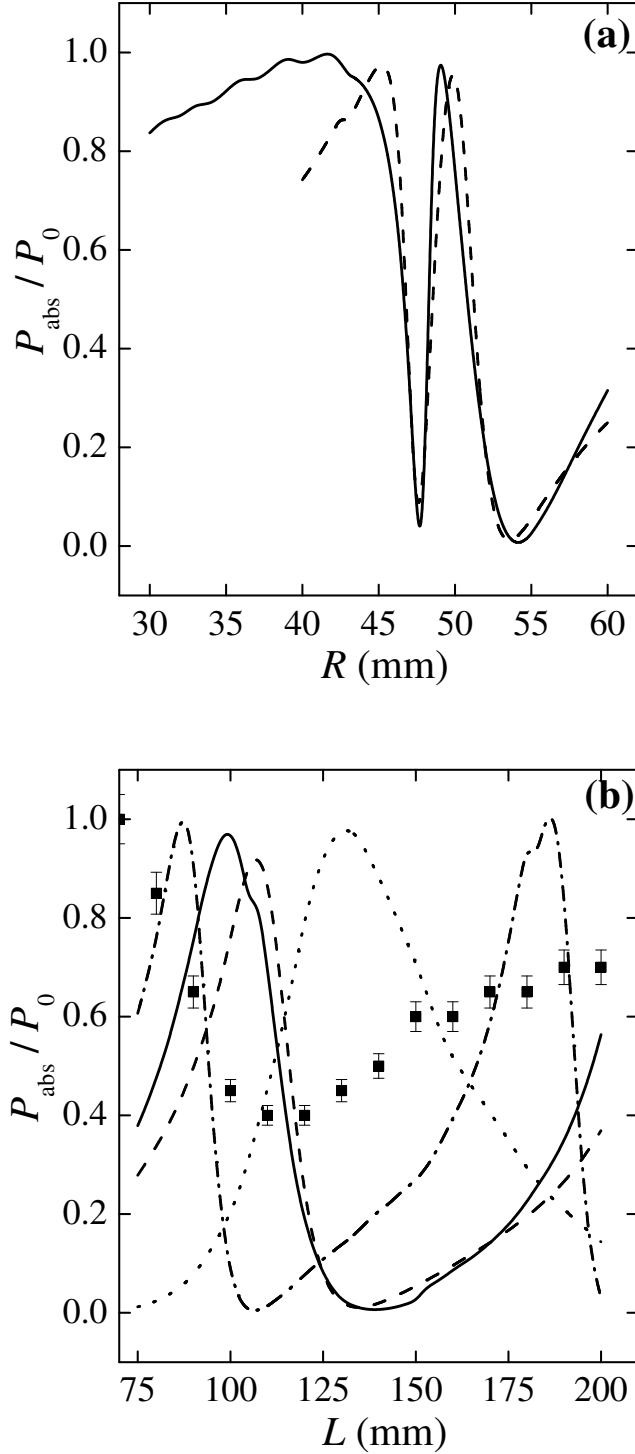
Fig. 5. Fractional average power absorbed by the plasma, as a function of R (a) and L (b), with all other reactor dimensions as in Fig. 1. The curves are simulation results obtained at $L = 150$ mm [in (a)] or $R = 50$ mm [in (b)], adopting the following electron density radial profiles [see Fig. 2(a)] at $n_{e,\text{max}} = 10^{15}$ cm^{-3}: hollow (solid), linear (dashed). The other curves in (b) are also simulations results obtained for the hollow n_e profile and the following values of R (in mm): 55 (dotted), 60 (dashed-dotted). The points in (b) are experimental results obtained at $P_0 = 600$ W and $R = 50$ mm.

Fig. 6. Contour-plot of the logarithm of the modulus of the total velocity (normalized to its maximum value), numerically calculated for the AIT-reactor represented in Fig. 1, adopting the hollow radial profile of the electron density [see Fig. 2(a)] at $n_{e,max} = 10^{15}$ cm^{-3}, $Q = 10^3$ sccm, and $T_{g_w} = 300$ K. The gradients of grey in background are for the intensity of $\mathbf{v}$, whereas the streamlines are for its direction.
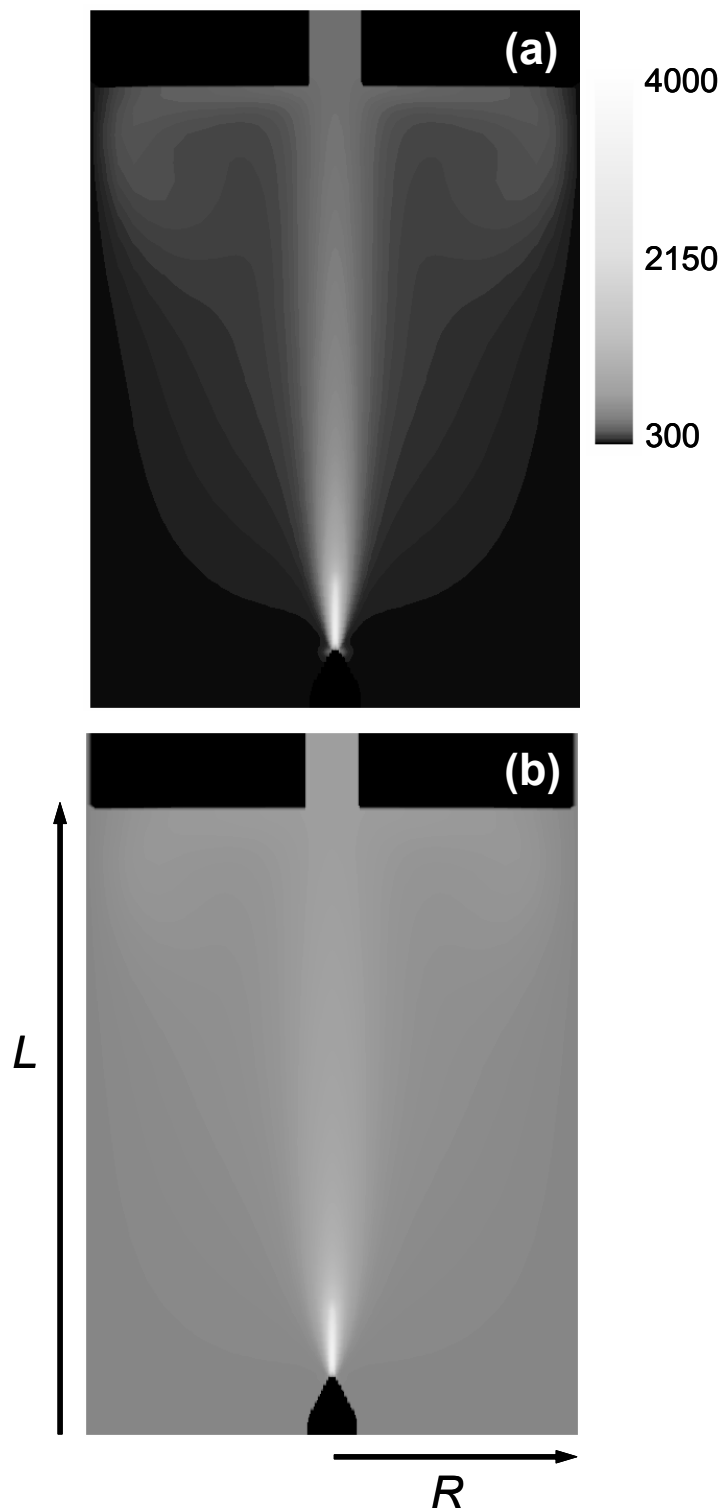
Fig. 7. Contour-plot of the gas temperature, numerically calculated for the AIT-reactor represented in Fig. 1, adopting the hollow radial profile of the electron density [see Fig. 2(a)] at $n_{e,\mathrm{max}} = 10^{15}$ cm^{-3}, $Q = 10^3$ sccm, and the following values of T_{g_w} (in K): 300 (a), 600 (b).
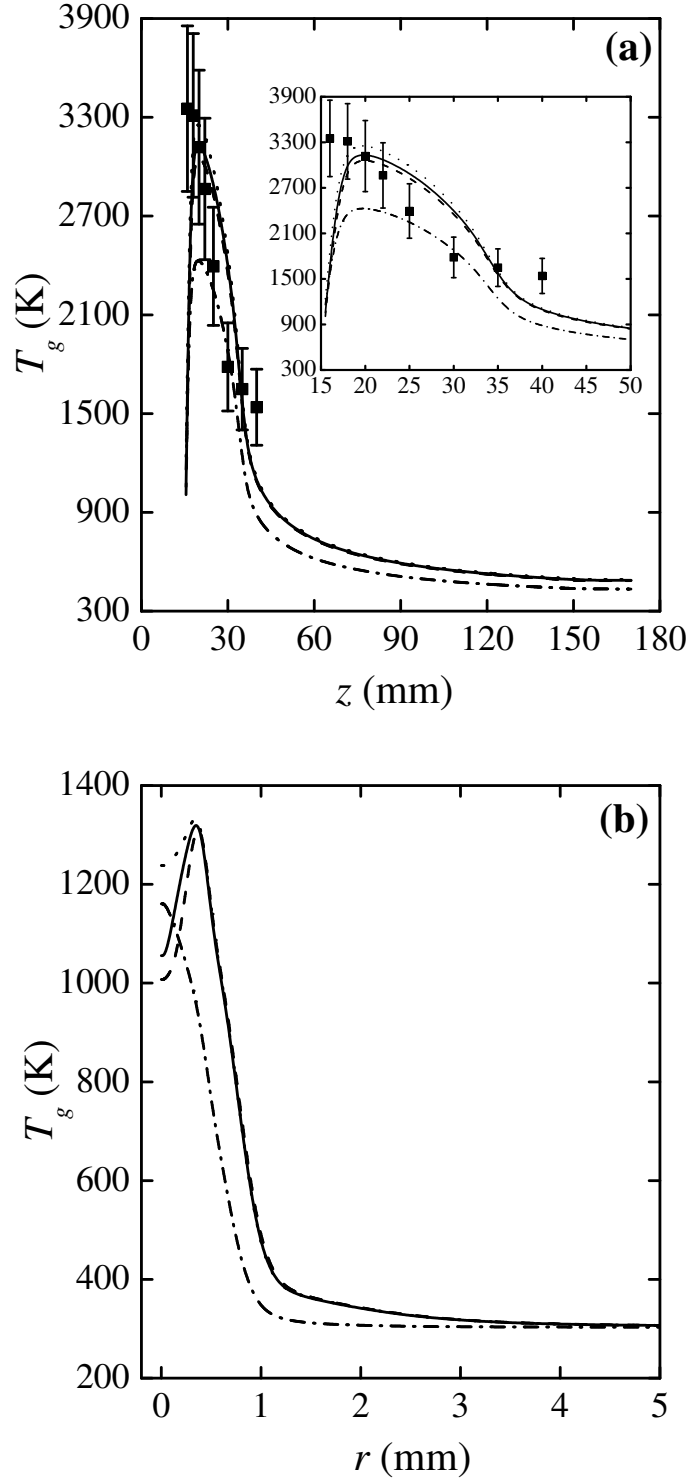
Fig. 8. Axial (at $r = 0$) (a) and radial (at $z = l_n$) (b) T_g profiles, for $Q = 10^3$ sccm. The curves are simulation results obtained at $T_{g_w} = 300$ K, adopting the following electron density radial profiles [see Fig. 2(a)] at $n_{e,\max} = 10^{15}$ cm^{-3}: hollow (solid), displaced hollow (dashed), flat (dotted), and linear (dashed-dotted). The points in (a) are experimental results (divided by a factor of 1.3 for representation purposes), obtained at $P_0 = 600$ W. The insert in Fig. 8(a) is just a zoom of this figure over the plasma region.